STRUCTURAL IDENTIFIABILITY-ORIENTED OFFLINE INERTIAL PARAMETER ESTIMATION FOR PMSM UNDER CONSTANT Q-AXIS CURRENT EXCITATION

Yuanyi LIU[1]

Accurate mechanical parameter estimation is essential for improving the control performance and stability of Permanent Magnet Synchronous Motor (PMSM) systems. Traditional identification methods based on sinusoidal excitation typically rely on injecting dual-frequency or dual-amplitude speed signals and performing segmented torque integration, which often requires precise speed tracking and inner-loop tuning. This paper proposes an alternative offline estimation method based on constant q-axis current excitation, which simplifies the excitation structure and estimation process. By applying a fixed current in the q-axis and integrating the electromagnetic torque over time, the proposed approach enables direct decoupling and estimation of inertia and damping-related parameters. Compared to the energy-based sinusoidal excitation method, this momentum-oriented strategy avoids dependence on tracking performance and improves robustness under varying system conditions. Simulation results demonstrate the effectiveness and reliability of the proposed method in achieving accurate mechanical parameter estimation with enhanced structural identifiability.

Keywords: PMSM, Mechanical parameter estimation, Constant q-axis current, Structural identifiability, Offline identification, Inertia estimation, Signal excitation method

1. Introduction

Permanent-magnet synchronous motors (PMSMs) are widely used in modern drives for their high torque density, efficiency, and fast dynamics [1-3]. Accurate mechanical parameters—the moment of inertia J, viscous damping B_m, and Coulomb friction C_m—govern torque response and closed-loop stability under varying operating conditions [4-5]. These data are seldom provided and may drift with wear, temperature, and disturbances, motivating robust identification strategies.

Two families dominate the literature. Online model-based estimators (e.g., EKF, RLS) allow in situ updates but are sensitive to noise and observer tuning [6-7]. Offline excitation-based methods offer repeatability and numerical stability; among them, sinusoidal-excitation schemes (dual-frequency or variable-amplitude) estimate J and damping via segmented energy/torque relations but depend on speed-

[1] Lingnan Normal University, School of Electronic and Electrical Engineering, Zhanjiang, 524048, China; e-mail: lyy_lou@163.com

loop tracking quality and careful signal design [8-10]. To enhance robustness while retaining identifiability, current-excitation has been explored. Prior studies reported current-based torque analyses and constant *d*-q injections [11-12], yet typically focus on inertia, require coordinated *d*/q currents, and rarely formalize structural identifiability.

This paper compares two offline strategies under identical conditions: (1) a sinusoidal-excitation baseline that estimates J, B_m, C_m using dual-amplitude speed commands with segmented torque integration; and (2) a constant q-axis current strategy that injects a fixed i_q and applies the impulse–momentum principle across acceleration, speed-hold, and coast-down phases, enabling single-run estimation of J, B_m, C_m without precise speed tracking or elaborate signal design. Structural identifiability is established under mild assumptions, and simulations on a surface-mounted PMSM (SPMSM) demonstrate improved accuracy and robustness over a broad speed range.

2. Mathematical Modeling and Vector Control of PMSM

This section introduces the core mathematical model of PMSM in the *d*-q reference frame and outlines the Field-Oriented Control (FOC) strategy, which are fundamental to high-performance motor control and parameter identification [13-14].

2.1 Mathematical Model of PMSM

The PMSM model in the *d-q* rotating frame is widely used for modern vector control. The stator voltage equations are expressed as:

$$u_d = R_s i_d + \frac{d\psi_d}{dt} - \omega_e \psi_q, \qquad u_q = R_s i_q + \frac{d\psi_q}{dt} + \omega_e \psi_d \tag{1}$$

where u_d, u_q denote *d*- and *q*-axis stator voltages, i_d, i_q represent the corresponding *d*-axis and *q*-axis stator currents, R_s is the stator winding resistance, and ω_e is the electrical angular velocity, ψ_d, ψ_q represent the stator flux linkages in the *d*-axis and *q*-axis, respectively.

The flux linkages in the stator windings are:

$$\psi_d = L_d i_d + \psi_f, \qquad \psi_q = L_q i_q \tag{2}$$

In these equations (2), L_d, L_q indicate the inductances along the *d*-axis and *q*-axis respectively, and ψ_f is the rotor magnet flux linkage. For SPMSMs, where saliency is negligible, the electromagnetic torque simplifies to:

$$T_e = \frac{3}{2} p_n \psi_f i_q \tag{3}$$

where p_n is the number of pole pairs and T_e the electromagnetic torque; the shaft dynamics are

$$J \frac{d\omega_m}{dt} = T_e - B_m \omega_m - C_m \text{sign}(\omega_m) - T_L \tag{4}$$

where ω_m is the rotor mechanical speed, T_L the external load torque, and sign (the sign function indicating the friction direction). This simplified model supports controller synthesis and underpins offline mechanical-parameter identification [15-16].

2.2 Field-Oriented Control (FOC) Strategy

FOC is adopted to decouple stator currents in the rotating d-q frame [17-18]. As shown in Fig. 1, a speed PI generates the torque-producing reference i_q^* with the field-orientation setpoint $i_d^*=0$; the inner d/q current PIs run with cross-coupling decoupling and anti-windup, and voltage commands are applied via SVPWM. This configuration is used throughout the paper. Representative FOC variants—maximum-torque-per-ampere (MTPA), field-weakening for operation above base speed (particularly for IPMSMs), unity-power-factor control, and zero d-axis current control for SPMSMs—are surveyed in [19-22] but are not required here.

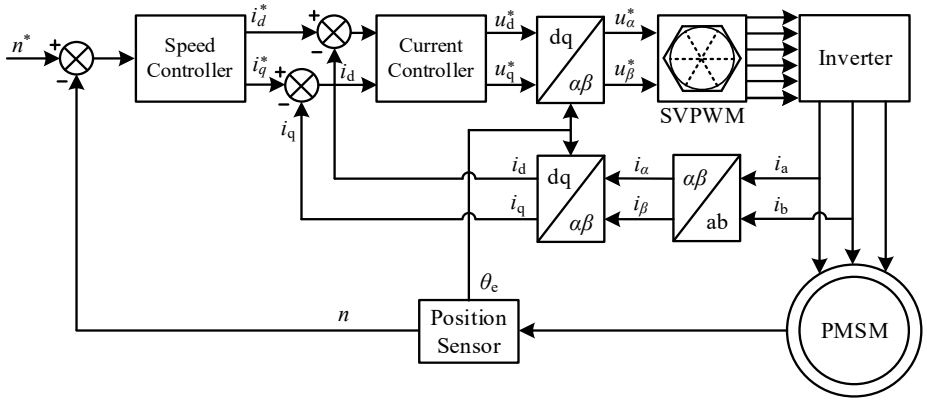

Fig. 1. Field-oriented control (FOC) architecture

2.3 Controller Configurations for the Two Methods

Method 1: Sinusoidal-excitation strategy. Within the FOC framework, a cascaded architecture is used. The outer speed loop is a PI regulator (K_{sp}, K_{si}) that tracks a sinusoidal speed command and produces the torque-generating reference i_q^*; the field-orientation setpoint is $i_d^*=0$. The inner d/q current loops use PI controllers with gains (K_{idp}, K_{idi}) and (K_{iqp}, K_{iqi}). Decoupling of cross-coupling terms and anti-windup back-calculation are enabled. Voltage commands are synthesized by SVPWM.

Method 2: Constant q-axis current strategy. The speed loop is disabled. The references are $i_d^*=0$ and a piecewise-constant i_q^* scheduled for acceleration, speed hold, and free deceleration. Only the inner d/q current PI loops (K_{idp}, K_{idi}), (K_{iqp}, K_{iqi}) operate under SVPWM, with the same decoupling and anti-windup as in Method 1. The rotor response over the three phases is recorded for parameter identification; the speed-loop gains (K_{sp}, K_{si}) are used only in Method 1.

Controller gains are computed from the plant data in Table 1 using a model-based loop-shaping guideline with bandwidth separation.

Table 1.

Electrical and mechanical parameters of the PMSM drive

Parameter	Symbol	Value	Unit	Parameter	Symbol	Value	Unit
DC bus voltage	U_{dc}	311	V	Permanent magnet flux linkage	ψ_f	0.175	Wb
Rated voltage	U_N	220	V	Number of pole pairs	p_n	5	—
Rated current	I_N	8	A	Moment of inertia	J	0.0023	kg·m²
Rated speed	n	1500	r/min	Viscous damping coefficient	B_m	0.002	N·m·s/rad
Stator resistance	R_s	1.180	Ω	Coulomb friction coefficient	C_m	0.35	N·m
Stator inductance	L_s	9.3462	mH				

With cross-coupling feedforward, each current axis behaves as a decoupled first-order loop; the *d*-q current PIs are tuned to a critically damped target at the chosen current-loop bandwidth. Anti-windup back-calculation is enabled, and voltages are applied via SVPWM. For Method 1, the speed PI is designed from the rigid-body speed channel using the torque constant obtained from the machine data, with a target bandwidth about one decade lower than the current loops to secure time-scale separation and a large phase margin. Method 2 disables the speed loop; the current-loop gains are identical to those of Method 1. Design formulas and the final gain values used in the simulations are listed in Table 2.

Table 2**.**

PI gains — analytical expressions and final values

Gain	Expression (continuous-time)	Design choice (ζ, ω)	Final value (Sinusoidal)	Final value (Constant i_q)
$\boldsymbol{K_{sp}}$	$(2\zeta_s\omega_s J - B_m)/K_t$	ζ_s=1.00, ω_s=628.318531 rad/s	2.200583	—
$\boldsymbol{K_{si}}$	$(\omega_s^2 J)/ K_t$	*same as above*	691.812270	—
$\boldsymbol{K_{idp}}$	$2\zeta_i\omega_{ci}L_s - R_s$	ζ_i=1.00, ω_{ci}=6283.185307 rad/s	116.267813	116.267813
$\boldsymbol{K_{idi}}$	$\omega_{ci}^2 L_s$	—	$3.689732e\times10^5$	3.689732×10^5
$\boldsymbol{K_{iqp}}$	$2\zeta_i\omega_{ci}L_s - R_s$	*same as* K_{idp}	116.267813	116.267813
$\boldsymbol{K_{iqi}}$	$\omega_{ci}^2 L_s$	—	$3.689732e\times10^5$	3.689732×10^5

3. Mechanical Parameter Identification in PMSM Using Sinusoidal Excitation

This section reviews a classical offline identification technique driven by sinusoidal speed commands, widely adopted in PMSM drives. Two speed references with the same electrical frequency and different amplitudes are applied in separate runs; by windowed integration of the electromagnetic torque over selected electrical-angle sectors, the method yields the mechanical parameters J, B_m and C_m [23-26].

3.1 Excitation-Induced Coupling and Identification

This method injects periodic speed references into the system, generating predictable and periodic electromagnetic torque responses. Under no-load conditions, the mechanical dynamic model of the PMSM can be simplified as:

$$T_{\mathrm{e}} = T_{\mathrm{J}} + T_{\mathrm{f}} = J\frac{d\omega_{\mathrm{m}}}{dt} + B_{\mathrm{m}}\omega_{\mathrm{m}} + C_{\mathrm{m}}\mathrm{sign}(\omega_{\mathrm{m}}) \tag{5}$$

where T_{J} is the inertia torque, and T_{f} represents the friction torque.

Assuming the rotor speed varies sinusoidally:

$$\omega_{\mathrm{m}} = A_{\mathrm{h}}\sin(\omega_{\mathrm{h}}t) \tag{6}$$

here, A_{h} represents the amplitude of the sinusoidal speed reference, and ω_{h} is its angular frequency. The corresponding torque components are:

$$T_{\mathrm{J}} = JA_h\omega_h\cos(\omega_h t), \qquad T_f = B_{\mathrm{m}}\omega_{\mathrm{m}} + C_{\mathrm{m}}\mathrm{sign}(\omega_{\mathrm{m}}) \tag{7}$$

Sinusoidal speed commands render the inertia torque (proportional to $d\omega_{\mathrm{m}}/dt$) and the friction torque (in phase with ω_{m}) as nearly orthogonal time-domain waveforms, which enables parameter separation by integrating the electromagnetic torque over selected rotor-angle sectors. As shown in Fig. 2, the rotor speed is sinusoidal (left); the inertia torque exhibits a cosine-like trace, the friction torque follows the sine-like speed, and the electromagnetic torque is their superposition (right). Windowed integration makes the energy contributions of each term distinguishable, allowing identification without additional sensors or high-rate acquisition.

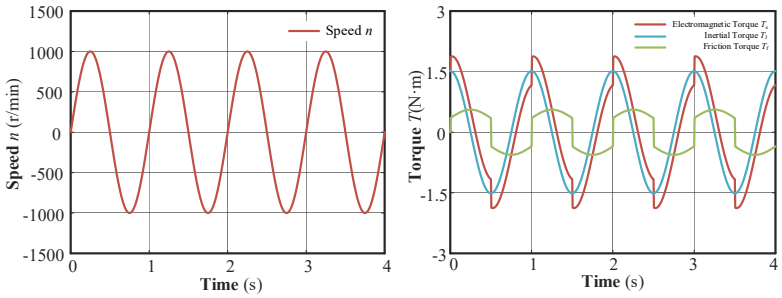

Fig. 2. Sinusoidal rotor speed (left) and torque components (right)

3.2 Time-Domain Integration and Parameter Estimation

To extract the values of the mechanical parameters, the electromagnetic torque response is integrated over specific intervals of the rotor electrical angle $\theta_{\mathrm{h}}=\omega_{\mathrm{h}}t$: [27-30]

First, over the interval : [-π/2, π/2]

$$\int_{-\frac{\pi}{2}}^{\frac{\pi}{2}} T_{\mathrm{e}}\mathrm{d}\theta = = \int_{-\frac{\pi}{2\omega_{\mathrm{h}}}}^{\frac{\pi}{2\omega_{\mathrm{h}}}} JA_{\mathrm{h}}\omega_{\mathrm{h}}\cos(\omega_{\mathrm{h}}t)\mathrm{d}t + \int_{-\frac{\pi}{2\omega_{\mathrm{h}}}}^{\frac{\pi}{2\omega_{\mathrm{h}}}} (B_{\mathrm{m}}A_{\mathrm{h}}\sin(\omega_{\mathrm{h}}t) + C_{\mathrm{m}}\mathrm{sign}(\sin(\omega_{\mathrm{h}}t)))\mathrm{d}t = 2JA_{\mathrm{h}} = K_a \tag{8}$$

where K_a represents the result of the integral derived from the above expression. Next, the electromagnetic torque is integrated over the interval [0, π], as shown below:

Then, over the interval: [0, π]

$$\int_0^{\pi} T_e \mathrm{d}\theta = = \int_0^{\frac{\pi}{\omega_h}} JA_h\omega_h \cos(\omega_h t)_j \mathrm{d}t + \int_0^{\frac{\pi}{\omega_h}} (B_m A_h \sin(\omega_h t) + C_m \mathrm{sign}(\sin(\omega_h t)))_f \mathrm{d}t = \frac{2}{\omega_h} B_m A_h + \frac{\pi}{\omega_h} C_m = K_b \quad (9)$$

where K_b represents the result of the integral derived from the above expression.

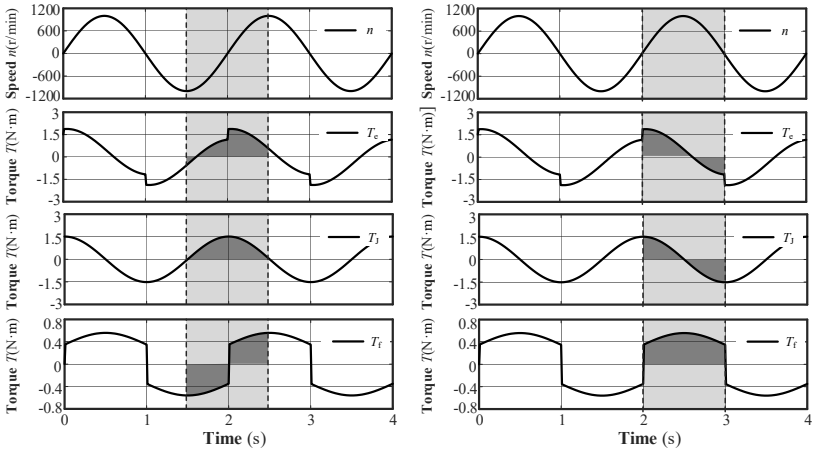

Fig. 3. Sinusoidal-excitation: windowed torque integrals: (left) [-π/2, π/2];(right) [0, π]

To resolve both B_m and C_m, two distinct sinusoidal speed references are introduced:

$$\omega_{m1} = A_{h1}\sin(\omega_h t), \qquad \omega_{m2} = A_{h2}\sin(\omega_h t) \quad (10)$$

According to equation (10), two distinct integral outcomes can be obtained as follows:

$$\int_0^{\frac{\pi}{\omega_h}} T_e \mathrm{d}t = \frac{2}{\omega_h} B_m A_{h1} + \frac{\pi}{\omega_h} C_m = K_{b1}, \qquad \int_0^{\frac{\pi}{\omega_h}} T_e \mathrm{d}t = \frac{2}{\omega_h} B_m A_{h2} + \frac{\pi}{\omega_h} C_m = K_{b2} \quad (11)$$

Based on equations (8) and (11), the mechanical parameters can be identified through the following derived expressions.

$$\hat{J} = \frac{K_a}{2A_h}, \qquad \hat{B}_m = \frac{\omega_h(K_{b2} - K_{b1})}{2(A_{h2} - A_{h1})}, \qquad \hat{C}_m = \frac{\omega_h(A_{h2}K_{b1} - A_{h1}K_{b2})}{\pi(A_{h2} - A_{h1})} \quad (12)$$

here, $\hat{J}$, $\hat{B}_m$ and $\hat{C}_m$ represent the estimated values of the rotational inertia, viscous damping coefficient, and Coulomb friction coefficient, respectively.

This enhanced strategy enables accurate and independent estimation of all three mechanical parameters by leveraging the orthogonality of torque components and the systematic variation of excitation amplitude.

3.3 Control Framework and Practical Guidelines

Sinusoidal-excitation identification procedure (Fig. 4).

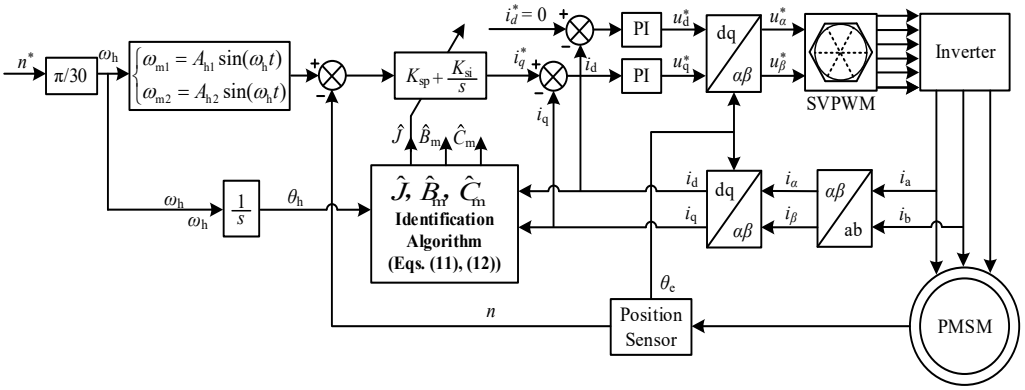

Fig. 4. Sinusoidal-excitation identification: control block diagram.

With i_d=0 and SVPWM modulation, two sinusoidal speed references of the same frequency but different amplitudes are applied in sequence. After each run, the electromagnetic torque is window-integrated to estimate J, B_m and C_m. Practical settings: (1) choose the excitation at 1-2 Hz (≈ one-tenth of the measured speed-loop bandwidth); the bandwidth can be obtained from a small-signal frequency-response test (-3 dB crossover) or inferred from the selected PI gains and the motor model—e.g., a 15 Hz speed bandwidth suggests an injection around 1.5 Hz; (2) ensure the two amplitudes differ by ≥10% to improve separability of the parameters; (3) avoid over-excitation to prevent controller saturation and nonlinear effects—constrain $|i_q|$≤0.7 p.u. and keep the speed-tracking error within 5% during injection. Under these settings the method is well suited to offline/commissioning tests in controlled conditions and does not require high-bandwidth sensors.

4. Mechanical Parameter Identification under Constant Current Excitation

4.1 Steady-State Torque Dynamics and Excitation Principle

According to the impulse-momentum theorem, the integral of an external torque over time equals the change in angular momentum:

$$\int_{t_1}^{t_2} T_e(t)\mathrm{d}t = J(\omega_m(t_2) - \omega_m(t_1)) \tag{13}$$

This highlights that net torque input causes changes in system momentum over a finite interval. Unlike traditional spatial-domain identification methods that rely on trajectory tracking accuracy, this approach emphasizes temporal impulse effects, thus improving robustness under relaxed control conditions.

4.2 Sequential Identification Procedure with Fixed Current Injection

Under no load (T_L=0), the test follows the command schedule in (14): set i_d^*=0 and apply a piecewise-constant q-axis current

$$i_d^*(t)=0,\quad i_q^*(t)=I_Q=\begin{cases} I_Q^{acc}, & t\in(t_1,t_2) \text{ (Phases I:acceleration)} \\ I_Q^{hold}, & t\in(t_3,t_4) \text{ (Phases II:hold)} \\ 0, & t\in(t_5,t_6) \text{ (Phases III:coast-down)} \end{cases} \tag{14}$$

SVPWM is active in Phases I-II and switched off at t=t_5 so the rotor coasts freely. In practice, $I_Q^{acc}$and $I_Q^{hold}$are chosen at (or near) the rated current to ensure sufficient excitation, though this is not mandatory. With i_d=0, (3) gives $T_e = K_t i_q$; hence the piecewise-constant i_q maps to piecewise-constant torque, shaping the speed response in Fig. 5.

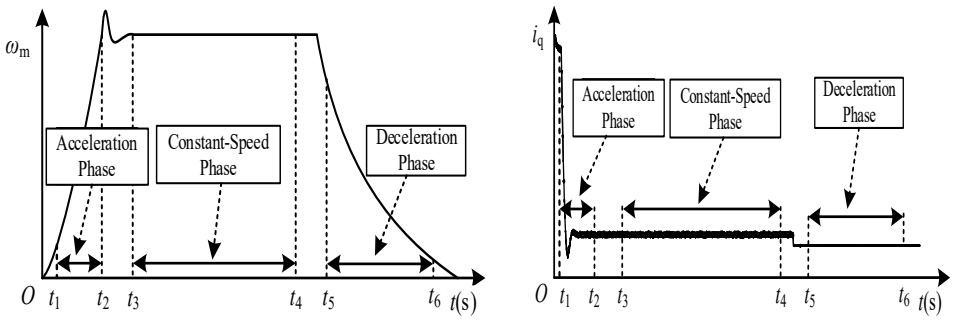

Fig. 5. Constant-current test: rotor speed ω_m(t)(left) and injected current i_q(t)(right), per (14)

Phase I: Acceleration-rotor accelerates due to positive electromagnetic torque. (Here $i_q = I_Q \Rightarrow T_e > 0$ by (3), yielding a positive slope in ω_m(t).)

Phase II: Speed holding-torque balances internal friction, speed remains nearly constant. (i_q remains I_Q; $T_e \approx$ friction torque, so $d\omega_m/dt \approx 0$.)

Phase III: Free deceleration-rotor slows down without external drive. (SVPWM off $\Rightarrow i_q$ =0, T_e = 0; ω_m(t) decays due to B_m and Coulomb friction C_m.)

To analyze the system dynamics over a specified interval [t_a, t_b], the momentum balance principle is applied. Given that the rotor speed ω_m remains strictly positive throughout the test duration, the mechanical dynamic equation (4) can be expressed in an integral form, which effectively captures the cumulative torque input as a torque impulse. Let $\Delta\omega_m$=$\omega_m(t_b)$-$\omega_m(t_a)$, $\Delta\theta_m$=$\theta_m(t_b)$−$\theta_m(t_a)$, and Δt=t_b−t_a, denote the rotor speed variation, angular displacement, and time interval length, respectively.

$$K=\int_{t_a}^{t_b} T_e(t)\mathrm{d}t = J\Delta\omega_m + B_m\Delta\theta_m + C_m\Delta t \tag{15}$$

Applying this expression to the three identification phases-acceleration (t_1,t_2), constant speed (t_3,t_4), and deceleration (t_5,t_6)-results in the following equation set:

$$\begin{cases} K_1 = J \cdot \Delta\omega_{m,1} + B_m \cdot \Delta\theta_{m,1} + C_m \cdot \Delta t_1 \\ K_2 = J \cdot \Delta\omega_{m,2} + B_m \cdot \Delta\theta_{m,2} + C_m \cdot \Delta t_2 \\ K_3 = J \cdot \Delta\omega_{m,3} + B_m \cdot \Delta\theta_{m,3} + C_m \cdot \Delta t_3 \end{cases} \tag{16}$$

The above set of linear equations can be expressed in compact matrix form:

$$\begin{bmatrix} K_1 \\ K_2 \\ K_3 \end{bmatrix} = \begin{bmatrix} \Delta\omega_{m,1} & \Delta\theta_{m,1} & \Delta t_1 \\ \Delta\omega_{m,2} & \Delta\theta_{m,2} & \Delta t_2 \\ \Delta\omega_{m,3} & \Delta\theta_{m,3} & \Delta t_3 \end{bmatrix} \cdot \begin{bmatrix} J \\ B_m \\ C_m \end{bmatrix} = A \cdot \begin{bmatrix} J \\ B_m \\ C_m \end{bmatrix} \tag{17}$$

Based on Equation (17), the mechanical parameter estimation results can be expressed as:

$$\left[\hat{J}, \hat{B}_m, \hat{C}_m\right]^T = \boldsymbol{A}^{-1}\left[K_1, K_2, K_3\right]^T \tag{18}$$

Link to (3) and Fig. 5 made explicit: Eq. (3) provides the torque-current relation ($T_e \propto i_q$ for i_d=0). Using the piecewise profile in (14), the constant positive torque during Phases I-II produces the rise/hold segments of ω_m(t) in Fig. 5, while i_q=0 in Phase III eliminates electromagnetic torque so that ω_m(t) decays under B_m and C_m only. This explicit mapping clarifies how the injected i_q(t) generates the speed evolution depicted in Fig. 5.

4.3 Existence and Uniqueness Conditions of the Solution

To ensure the validity of the proposed identification algorithm, it is essential to establish the existence and uniqueness conditions of the solution to the parameter estimation model. As derived in Equation (18), the identification problem can be represented as a system of linear equations:

$$\boldsymbol{K} = \boldsymbol{A} \cdot \boldsymbol{x} \tag{19}$$

where $\boldsymbol{x}$ = [$\hat{J}$, $\hat{B}_m$, $\hat{C}_m$]^T is the vector of unknown mechanical parameters, $\boldsymbol{K} \in \mathbb{R}^{3\times1}$ is the vector of integrated electromagnetic torques over distinct time intervals, and $\boldsymbol{A} \in \mathbb{R}^{3\times3}$ is the coefficient matrix constructed from measured variations of rotor speed, displacement, and time duration in three distinct operating phases: acceleration, constant-speed, and deceleration.

According to the basic theory of linear systems, Equation (19) has a unique solution if and only if the matrix A is nonsingular, i.e.:

$$\det(\boldsymbol{A}) \neq 0 \Leftrightarrow rank(\boldsymbol{A}) = 3 \tag{20}$$

To verify the existence and uniqueness of the solution for the parameter identification problem, it is necessary to examine the linear independence of the rows of the coefficient matrix $\boldsymbol{A}$. Let the three rows of $\boldsymbol{A}$ be denoted as $\boldsymbol{v}_1$, $\boldsymbol{v}_2$ and $\boldsymbol{v}_3$, respectively:

$$\boldsymbol{A} = \begin{bmatrix} \boldsymbol{v}_1 \\ \boldsymbol{v}_2 \\ \boldsymbol{v}_3 \end{bmatrix} = \begin{bmatrix} \Delta\omega_{m,1} & \Delta\theta_{m,1} & \Delta t_1 \\ \Delta\omega_{m,2} & \Delta\theta_{m,2} & \Delta t_2 \\ \Delta\omega_{m,3} & \Delta\theta_{m,3} & \Delta t_3 \end{bmatrix} \tag{21}$$

Assume that there exists a set of real coefficients $(\lambda_1, \lambda_2, \lambda_3) \in \mathbb{R}^3$, not all zero, such that:

$$\lambda_1 \boldsymbol{v}_1 + \lambda_2 \boldsymbol{v}_2 + \lambda_3 \boldsymbol{v}_3 = 0 \tag{22}$$

This homogeneous system admits only the trivial solution $\lambda_1=\lambda_2=\lambda_3$ if and only if the vectors $\{\boldsymbol{v}_1, \boldsymbol{v}_2, \boldsymbol{v}_3\}$ are linearly independent. Therefore, matrix $\boldsymbol{A}$ is nonsingular, and the solution to the parameter identification problem is guaranteed to be unique. As shown in Table 3, the acceleration, constant-speed, and deceleration phases represent three physically independent modes of motion, with distinct signs and magnitudes of angular speed variations. Given that each phase corresponds to a unique dynamic behavior, the associated rows of matrix $\boldsymbol{A}$ are linearly independent. Therefore, we conclude that $\det(\boldsymbol{A}) \neq 0$, ensuring the uniqueness of the parameter identification solution.

Table 3

Physical Definitions and Motion Phases in Parameter Identification

Symbol & Condition	Motion Phase	Physical Interpretation
$\Delta\omega_{m,1} > 0$	Acceleration	Positive angular acceleration
$\Delta\omega_{m,2} \approx 0$	Constant speed	Angular acceleration approaches zero
$\Delta\omega_{m,3} < 0$	Deceleration	Negative angular acceleration
$\Delta\theta_{m,i} > 0$, $\Delta t_i > 0$	All phases	Displacement and time are always positive

4.4 Integrated Solution for Mechanical Parameter Identification Strategy

To demonstrate the engineering applicability of the proposed method, the overall identification strategy is illustrated by the system-level control block diagram presented in Fig. 6. This framework depicts a mechanical parameter identification process based on constant current excitation.

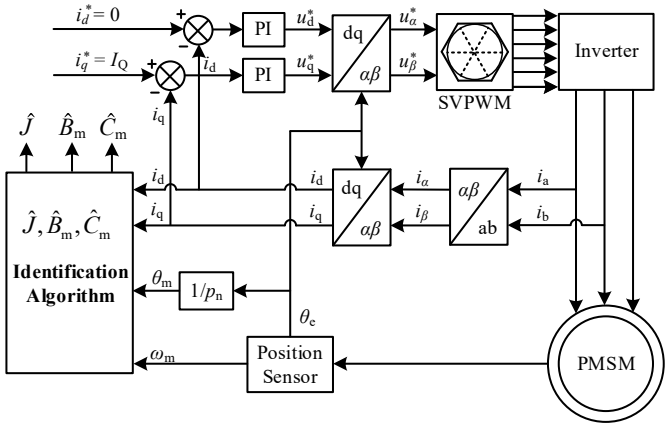

Fig. 6. Block diagram of the proposed constant-current identification scheme

The strategy operates under an open-loop scheme, where the d-axis reference current is set to zero ($i_d^*=0$) and a constant q-axis current (i_q^*=const) is injected, implemented within a Space Vector Pulse Width Modulation (SVPWM) framework. In the revised implementation, the q-axis current is scheduled in a piecewise-constant manner (see (14)): an acceleration level I_Q^{acc} in Phase I, a holding level I_Q^{hold} in Phase II, and zero in Phase III. Initially, the stator windings are energized with a rated q-axis current, generating a unidirectional electromagnetic torque that accelerates the rotor. After the rotor reaches the target speed at the end of Phase I, SVPWM remains enabled and i_q is held at I_Q^{hold} so that the electromagnetic torque balances mechanical losses ($T_e \approx B_m\omega_m+C_m$); this produces the nearly constant-speed segment in Fig. 5 (Phase II). Only after this short dwell is completed do we disable the PWM to initiate Phase III, during which the rotor freely decelerates due to internal losses.

Throughout this excitation and free-response process, key system variables-such as the three-phase stator currents, rotor speed, and angular position-are sampled in real time. The identification algorithm then processes this integrated dataset, spanning the acceleration, speed-holding, and deceleration phases, to estimate the mechanical parameters. For clarity and traceability, the commanded waveform $i_q(t)$ corresponding to Phases I-III (Fig. 5(right)) is recorded together with $\omega_m(t)$ (Fig. 5(left)), and the phase intervals (t_1,t_2), (t_3,t_4), (t_5,t_6) are used in the integral relations of (15)-(18).

Notably, the method completes the parameter identification in a single operation cycle, yielding accurate estimates of the moment of inertia $\hat{J}$, viscous damping coefficient $\hat{B}_m$, and Coulomb friction coefficient $\hat{C}_m$. It does not rely on pre-identified system parameters, speed feedback loops, or trajectory tracking algorithms. Instead, it capitalizes on the intrinsic system response to a standardized input. Compared with an "accelerate-then-immediately-disable" sequence, the explicit Phase-II dwell with $i_q= I_Q^{hold}$ improves repeatability and avoids transients contaminating the deceleration data set.

The proposed strategy exhibits strong robustness and algorithmic stability. Since the identification process is confined to the current control layer, it remains unaffected by outer-loop dynamics and avoids noise amplification typically associated with speed estimation. The identification accuracy is primarily influenced by three factors: the precision of current and speed sensors, the sampling rate synchronized with the microcontroller's oscillator, and the accuracy of the flux linkage estimation. In practice, we constrain $|i_q|\leq 0.7$ p.u. during Phases I-II and ensure the voltage commands stay within the linear SVPWM region to prevent saturation and nonlinear distortion.

In conclusion, the proposed algorithm offers an efficient, non-invasive, and practical solution for offline mechanical parameter identification. It is particularly suited for applications such as initial motor startup calibration, control parameter tuning, and dynamic modeling of motor-drive systems.

5. Simulation Results and Performance Evaluation

5.1 Simulation Verification of the Sinusoidal Excitation-Based Method

The two offline strategies are assessed in MATLAB/Simulink with a PMSM servo-drive model; this subsection reports the sinusoidal-excitation case. A low-frequency command $n(t) = n_A sin(2\pi ft)$ with $n_A \in \{1000,1300\}$ r/min and f=2Hz is applied to the speed loop. Identification proceeds in two stages: [0, 3] s for the inertia J and [3, 4.5] s for the viscous damping B_m and Coulomb friction C_m. The total run is 5 s. The measured speed tracks the reference tightly (Fig. 7, left), while the error remains small (Fig. 7, right), indicating adequate excitation and a properly tuned loop for reliable mechanical-parameter estimation.

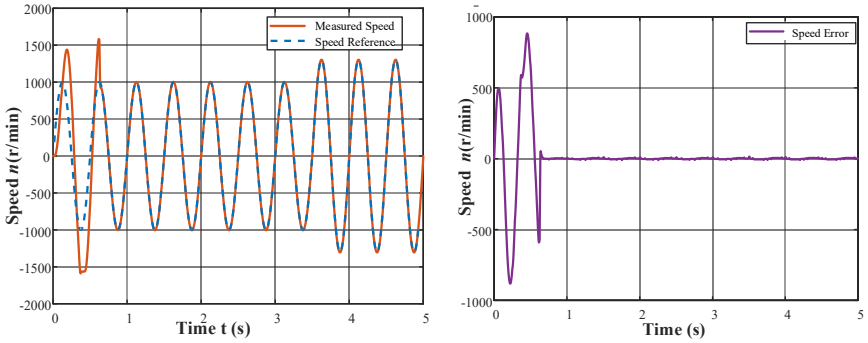

Fig. 7. Left: rotor speed tracking under a sinusoidal reference; right: rotor speed tracking error

During the sinusoidal-excitation test (f=2Hz, i_d^*=0), the stationary-frame SVPWM references u_α, u_β are zero-mean and remain within the linear-modulation range (Fig. 8, left), confirming unsaturated command injection. The d-q currents are consistent with these commands (Fig. 8, right): i_d is tightly regulated around zero, indicating proper field orientation and adequate inner-loop bandwidth, while i_q provides the torque-producing component required by the speed loop.

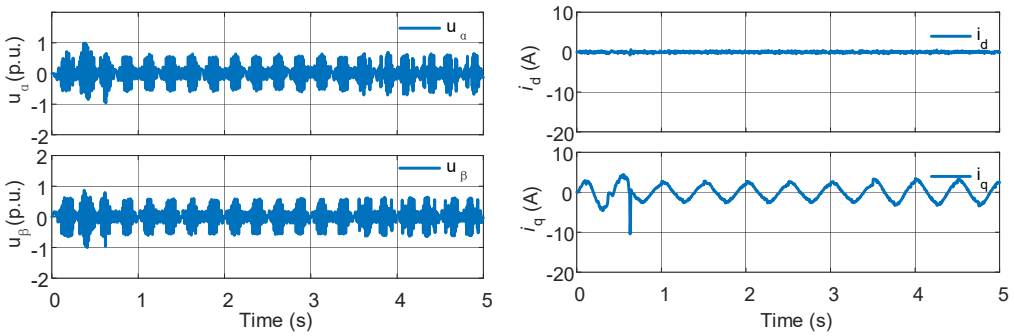

Fig. 8. Left: stationary-frame SVPWM references; right: *d*-q current responses(i_d^*=0)

Fig. 9 summarizes the sinusoidal-excitation run. In accordance with (11), the estimator integrals K_{b1} and K_{b2} accumulate only within their half-period windows [3.00, 3.25]s and [4.00, 4.25]s, respectively, and remain essentially zero elsewhere. The end-of-window plateaus are then used in (12) for parameter estimation (Fig. 9, left). The torque traces (electromagnetic, inertial, and friction) in Fig. 9 (right) reveal the distribution of effort and the energy exchange during identification, clarifying the mechanical response of the PMSM drive.

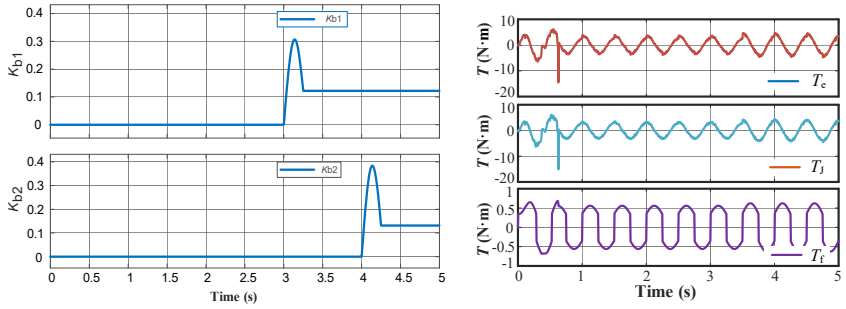

Fig. 9. Left: estimator integrals K_{b1}, K_{b2} under sinusoidal excitation; right: torque components vs. time

Fig. 10 shows the convergence of the identified mechanical parameters in the PMSM drive: inertia J, viscous damping B_m, and Coulomb friction C_m settle to their true values with decaying transients, indicating a stable estimator under sinusoidal excitation. To refine accuracy, the conventional sinusoidal-excitation offline method is run iteratively; Table 4 reports estimates and relative errors over three iterations. Final (3rd)-iteration errors are all within 4.0%; inertia achieves <0.3%, the damping error improves from −7.0% to −3.60%, and friction converges to 2.86%. These results verify the method's effectiveness under well-controlled excitation and tracking.

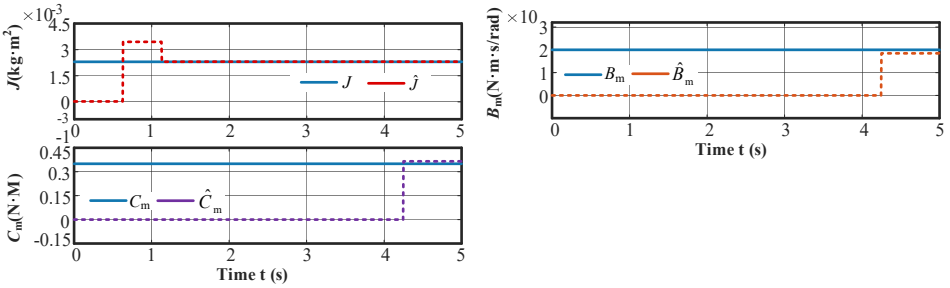

Fig. 10. Sinusoidal-excitation method: convergence of mechanical-parameter estimates

Table 4.

Sinusoidal method—results and errors (3 iterations)

Parameter	True Value	Iteration 1	Relative Error 1	Iteration 2	Relative Error 2	Iteration 3	Relative Error 3
J (kg·m²)	0.0023	0.002291	-0.391%	0.002308	0.348%	0.002306	0.261%
B_m (N·m·s/rad)	0.002	0.00186	-7.000%	0.001975	-1.25%	0.001928	-3.60%
C_m (N·m)	0.35	0.364120	4.031%	0.3542	1.20%	0.360012	2.86%

5.2 Simulation Validation of the Constant Current Excitation-Based Identification Strategy

Under the constant-current strategy ($i_d^*=0$, $i_q^*=i_{qN}$), a rated i_q injection first accelerates the rotor, then the drive holds a short steady-speed phase before the inverter is switched off at $t=1$ s to allow natural run-down. The identification completes in about 1.85 s, with segments of 0.05 s (acceleration), 1.00 s (speed hold), and 0.85 s (free deceleration). The electromagnetic-torque trace exhibits the expected rise-hold-decay pattern (Fig. 11, left), while the speed trajectory captures the full accelerate–coast–decay process (Fig. 11, right), providing clean data windows for subsequent parameter estimation.

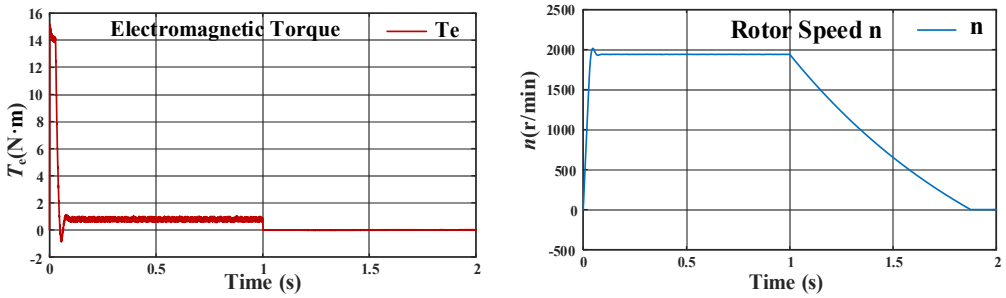

Fig. 11. Left: electromagnetic torque T_e; right: rotor speed n under constant-i_q excitation($i_d^*=0$, $i_q^*=i_{qN}$)

Fig. 12 summarizes the constant-i_q run. The mechanical angle θ_m exhibits the expected acceleration–hold–decay evolution (Fig. 12, left). With $i_d^*=0$ and a step $i_q^*=i_{qN}$, the stationary-frame SVPWM references u_α, u_β remain zero-mean within the linear-modulation range during acceleration and speed hold, then smoothly collapse after the inverter is disabled at $t=1$ s, indicating entry into free

deceleration (Fig. 12, right). This confirms that the commanded excitation is applied faithfully without saturation.

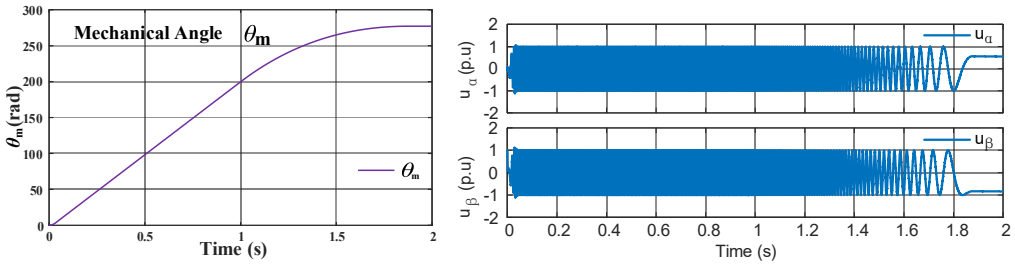

Fig. 12. Left: mechanical angle θ_m; right: stationary-frame SVPWM references u_α, u_β

Fig. 13 summarizes the constant-current test. With constant-i_q injection (i_d^*=0, i_q^*=i_{qN}), i_d is held near zero, indicating correct field orientation and adequate inner-loop bandwidth. The i_q current steps to the command, remains nearly constant during the hold phase, and drops to approximately zero immediately after the inverter is disabled at t=1s; no current saturation is observed (Fig. 13, left). The windowed torque integrals K_1-K_3 are shown (Fig. 13, right): each integral accumulates only within its designated window ([t_1,t_2] acceleration, [t_3,t_4] speed hold, [t_5,t_6] coast-down) and stays flat elsewhere. The end-of-window plateaus are substituted into (18) to solve for J, B_m, and C_m. In this run, K_1 captures the spin-up impulse, K_2 reflects the steady opposing torques during the hold, and K_3 records residual losses in coast-down, which confirms correct windowing and sufficient excitation.

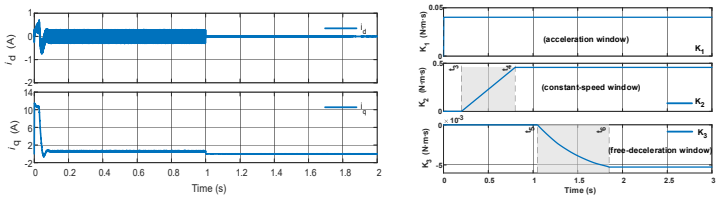

Fig. 13. Left: i_d and i_q under constant-i_q injection; right: windowed torque integrals K_1–K_3

Fig. 14 consolidates the constant-current identification run: torque, speed, and position responses together with the time histories of the parameter estimates. Table 5 quantifies performance; all three parameters are recovered with very small deviations (maximum≈0.087% for J; B_m 0.050%; C_m 0.0031%), indicating a numerically stable estimator. Compared with the sinusoidal baseline, the constant-current strategy exhibits higher accuracy and robustness under well-controlled excitation and tracking.

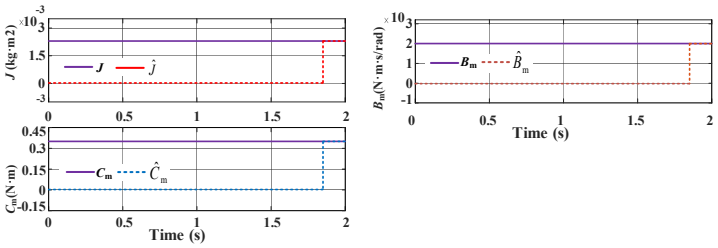

Fig. 14. Constant-current identification: convergence of mechanical-parameter estimates

Table 5

Constant-current method—results and errors

Parameter	True Value	Identified Value	Relative Error
J (kg·m²)	0.0023	0.002298	-0.0870%
B_m (N·m·s/rad)	0.002	0.002001	0.0500%
C_m (N·m)	0.35	0.349989	-0.0031%

5.3 Comparative Analysis of the Two Identification Strategies

Fig. 15 (left) compares the two strategies on a common scale by normalizing each identified parameter (J, B_m and C_m) to its true value. Under the common normalization, the constant-i_q scheme keeps all parameter estimates near 1.0 (close to the true values). In particular, the relative error of J is < 0.3%, and the errors of B_m and C_m are uniformly smaller than those of the sinusoidal baseline. Fig. 15 (right) shows that the sinusoidal baseline exhibits larger deviations and stronger fluctuations, especially in damping and friction, indicating weaker dynamic sensitivity and robustness. These results indicate that optimized excitation and adaptive estimation improve accuracy and stability.

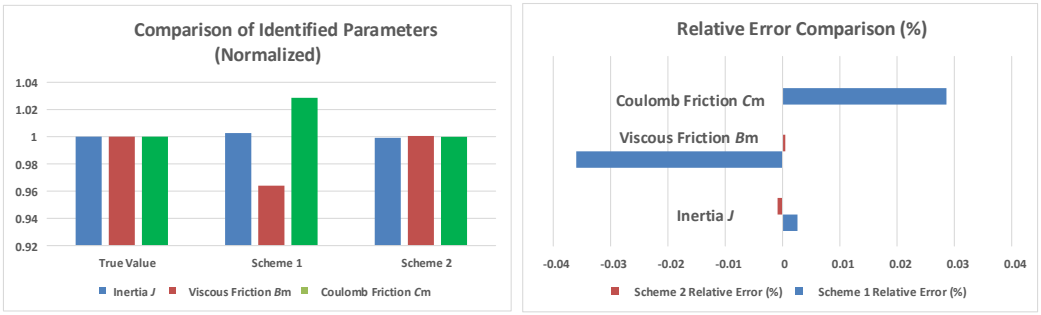

Fig. 15. Normalized parameters (left) and relative errors (%) (right) for the two methods.

6. Conclusions

This paper presented a comparative analysis of two offline mechanical parameter identification strategies for PMSMs. The first approach, widely adopted in literature, is based on sinusoidal speed excitation and employs torque integration under dual-amplitude input signals. Although effective under precise tracking

conditions, its robustness is limited by sensitivity to control loop tuning and excitation signal design.

To address these issues, a novel identification strategy based on constant q-axis current excitation was proposed. By injecting a fixed current and analyzing the electromagnetic torque response in the time domain, this method enables decoupled identification of inertia and friction parameters, avoiding the need for speed feedback or excitation optimization. Simulation results demonstrate that the proposed strategy achieves high accuracy, with relative errors below 0.1% for all parameters. It also exhibits strong robustness and structural identifiability under varying operating conditions. Owing to its simplicity, fast execution, and independence from outer-loop controllers, the proposed method is well suited for practical applications such as motor commissioning, controller initialization, and system modeling.

Acknowledgements

This work is supported by Special projects in key fields for higher education of Guangdong province [grant number 2021ZDZX3008].

REFERENCES

[1] P. Vas, Sensorless Vector and Direct Torque Control, Oxford University Press, Oxford, 1998.
[2] T. J. E. Miller, Brushless Permanent-Magnet and Reluctance Motor Drives, Oxford University Press, Oxford, 1989.
[3] S. Morimoto, M. Sanada, Y. Takeda, "Wide-speed operation of interior permanent magnet synchronous motors with high-performance current regulator," IEEE Trans. Ind. Appl., vol. 30, no. 4, pp. 920–926, 1994.
[4] K. Rajashekara, "Sensorless control of AC motor drives," IEEE Trans. Ind. Electron., vol. 53, no. 2, pp. 396–403, 2006.
[5] B. K. Bose, Modern Power Electronics and AC Drives, Prentice Hall, Upper Saddle River, NJ, 2002.
[6] H. Kubota, K. Matsuse, T. Nakano, "DSP-based speed adaptive flux observer of induction motor," IEEE Trans. Ind. Appl., vol. 29, no. 2, pp. 344–348, 1993.
[7] P. García, J. A. Pombo, C. Blanco, A. Arias, "Parameter identification of induction motors using RLS algorithm and on-line data," IEEE Trans. Energy Convers., vol. 14, no. 3, pp. 381–387, 1999.
[8] A. Consoli, A. Testa, G. Scarcella, "Online parameter estimation of induction machines by torque ripple minimization," IEEE Trans. Ind. Appl., vol. 35, no. 1, pp. 81–87, 1999.
[9] F. Scapino, M. Mengoni, L. Zarri, A. Tani, "Mechanical parameter identification of synchronous motors using torque and position sensors," IEEE Trans. Ind. Appl., vol. 54, no. 5, pp. 4987–4996, 2018.
[10] C. Zhang, Y. Yan, Q. Lu, "Mechanical parameter estimation of PMSM based on dual amplitude sinusoidal excitation," Proc. CSEE, vol. 35, no. 6, pp. 1413–1420, 2015.
[11] S. Bolognani, M. Zigliotto, M. Sandre-Haraldsen, "On-line mechanical parameter estimation for sensorless vector-controlled PMSM drives," IEEE Trans. Power Electron., vol. 25, no. 3, pp. 589–596, 2010.
[12] H. Ren, X. Wang, Y. Liu, Inertia identification for PMSM based on constant d–q current injection, Journal of Electrical Engineering & Technology, vol. 16, no. 1, pp. 59–66, 2021.
[13] Mesbahi A, Aljarhizi Y, Hassoune A, Khafallah M, Alibrahmi E. Boost converter implementation for wind generation system based on a variable speed PMSG. Proc. 2020 1st Int. Conf. Innovative Research in Applied Science and Engineering Technology (IRASET), IEEE, 2020: 1–6.

[14] He S, Wang M. Grey prediction PI control of direct drive permanent magnet synchronous wind turbine. Proc. 2020 IEEE 4th Conf. Energy Internet and Energy System Integration (EI2), IEEE, 2020: 2032–2035.
[15] Liu Y F, Zou M, Wang Y, Feng M K, Xu J Z, Jia X F, Zhao C Y. Modeling method of electromagnetic transient for PMSM oriented to offshore wind simulation. Trans. China Electrotech. Soc., 2024, 39(8): 2400–2411.
[16] Chen J, Ren Y F, Meng Q T, Xue Y, He J W. Sub-synchronous oscillation suppression strategy for direct-drive PMSM-based grid-forming wind turbines with UDE damping branch. Trans. China Electrotech. Soc., 2024, 39(7): 1985–2000.
[17] Wang D S, Yan X W, Jia J X, Li R B, Li T C. Continuous fault ride-through control strategy for direct-drive permanent magnet wind turbines based on virtual synchronous generator. Proc. CSEE, 2022, 42(6): 2164–2175.
[18] Bao G, Li Y, He X, et al. Virtual synchronization control strategy of direct drive permanent magnet wind turbine under load shedding operation mode. Proc. 2019 IEEE Int. Conf. Robotics and Biomimetics (ROBIO), IEEE, 2019: 2263–2268.
[19] Sun X.-D., Su Z.-H., Lei G., Yao M. “Robust Predictive Cascaded Speed and Current Control for PMSM Drives Considering Parameter Variations,” IEEE Transactions on Industrial Electronics, 71(9), pp. 10235–10245, Sep. 2024. doi:10.1109/TIE.2023.3337498.
[20] Wang Q., Wang G., Zhao N., Zhang G., Cui Q., Xu D. “An Impedance Model-Based Multiparameter Identification Method of PMSM for Both Offline and Online Conditions,” IEEE Transactions on Power Electronics, 36(1), pp. 727–738, Jan. 2021. doi:10.1109/TPEL.2020.3000896.
[21] Yang S.-M., Lin K.-W. “Automatic Control Loop Tuning for Permanent-Magnet AC Servo Motor Drives,” IEEE Transactions on Industrial Electronics, 63(3), pp. 1499–1506, Mar. 2016. doi:10.1109/TIE.2015.2477275.
[22] Erturk Ö., Akin B. “Inertia Estimation and Speed Loop Auto-Tuning for IPMSM Self-Commissioning,” IEEE Transactions on Energy Conversion, 34(3), pp. 1706–1714, Sep. 2019. doi:10.1109/TEC.2019.2915056.
[23] Lu W.-Q., Tang B., Ji K.-H., Lu K.-Y., Wang D., Yu Z.-J. “A New Load Adaptive Identification Method Based on an Improved Sliding Mode Observer for PMSM Position Servo System,” IEEE Transactions on Power Electronics, 36(3), pp. 3211–3223, Mar. 2021. doi:10.1109/TPEL.2020.3016713.
[24] Liu H., Tian D.-W., Wang Y.-Q., Liu H.-Y., Zhao S.-F., Wu Z.-Y. “Model-Compensated Active Disturbance Rejection Control for PMSM Based on Parameters Identification,” Proceedings of the 8th International Conference on Robotics, Control and Automation (ICRCA 2024), Chongqing, China, 5–7 Jul. 2024, pp. 318–324
[25] Tang S.-P., Cao Y.-F., Shi T.-N., Yan Y., Xia C.-L. “Online Estimation of Load Torque and Moment of Inertia Incorporating Extended Disturbance Observer With Trigger,” IEEE Transactions on Power Electronics, 40(4), pp. 5731–5742, 2025.
[26] Tang S., Cao Y., Shi T., Yan Y., Xia C. “Simultaneous Identification of Load Torque and Moment of Inertia of PMSM Based on Variable Structure Extended Sliding Mode Observer,” IEEE Transactions on Power Electronics, 39(7), pp. 8585–8596, Jul. 2024.
[27] Bolognani S, Zigliotto M. Parameter estimation of synchronous motors based on signal injection and observer design. IEEE Trans. Ind. Electron., 1999, 46(1): 139–144.
[28] T. M. Wolbank, R. W. De Doncker, “High frequency signal injection for sensorless control of AC machines at zero and low speed,” *IEEE Transactions on Industry Applications*, vol. 39, no. 6, pp. 1665–1671, 2003.
[29] Shi H L, Wang L H, Yang J, Lin S Y. Identification of PMSM mechanical parameters based on improved integration method under sinusoidal excitation. Trans. China Electrotech. Soc., 2023, 38(1): 102–109.
[30] Robinson E I, Okolo W A. Estimation of Permanent Magnet Synchronous Motor Parameters using a Linear Unknown Input Interval Observer. NASA Tech. Rep., 2021.